Mechanisms of Stress- and Fluid-Pressure-Driven Fault Reactivation in Gonghe Granite: Implications for Injection-induced Earthquakes

Chongyuan Zhang[1, 2], Dongjue Fan[1, 3], Derek Elsworth[4], Xingguang Zhao[5], Chun Zhu[6], Manchao He[2], Hao Zhang[1]

[1] Institute of Geomechanics, Chinese Academy of Geological Sciences, Beijing, 100081, China

[2] School of Mechanics and Civil Engineering, China University of Mining and Technology, Beijing 100083, China

[3] School of Civil and Resource Engineering, University of Science and Technology Beijing, Beijing, 100081, China

[4] Energy and Mineral Engineering, EMS Energy Institute and G3 Center, Pennsylvania State University, University Park, 16802, USA

[5] CNNC Key Laboratory on Geological Disposal of High-level Radioactive Waste, Beijing Research Institute of Uranium Geology, Beijing 100029, China

[6] School of Earth Sciences and Engineering, Hohai University, Nanjing, 210098, China

Corresponding author: Chongyuan Zhang (zhchongyuan@126.com, zhangchy@cags.ac.cn)

Key Points:

- The mechanism of fault slip in stress- and fluid-pressure-driven frictional slip experiments on granite faults is demonstrated
- By modifying the slip weakening criterion, a slip friction criterion considering friction strengthening and fault angle is established
- Fault activation mechanism and the influence of fault permeability on fracture overpressure during fluid injection have been studied

Abstract

We explore the impacts of stress- and fluid-pressure-driven frictional slip on variably roughened faults in Gonghe granite (Qinghai Province, China). Slip is on an inclined fault under simple triaxial stresses with concurrent fluid throughflow allowing fault permeability to be measured both pre- and post-reactivation. Under stress-drive, smooth faults are first slip-weakening and transition to slip-strengthening with rough faults slip-strengthening, alone. A friction criterion accommodating a change in friction coefficient and fault angle is able to fit the data of stable-slip and stick-slip. Under fluid-pressure-drive, excess pore pressures must be significantly larger than average pore pressures suggested by the stress-drive-derived failure criterion. This overpressure is conditioned by the heterogeneity of the pore pressure distribution in radial flow on the fault and related to the change in permeability. Fault roughness impacts both the coefficient of friction and the permeability and therefore exerts important controls in fluid-injection-induced earthquakes. The results potentially improve our ability to assess and mitigate the risk of injection-induced earthquakes in EGS.

Plain Language Summary

Enhanced geothermal systems (EGS) inject large amounts of fluid into a rock mass, leading to the slip of faults in the strata and thus causing earthquakes. Unlike the US and European EGS, many geothermal fields are located in seismically active areas with high tectonic stress levels in Western China, such as the Gonghe EGS. However, the mechanism of injection-induced seismicity under a high tectonic stress is still unclear. Herein, we report the results obtained from frictional slip tests under stress- and fluid-pressure-driven conditions in granite faults. Our results show that the slip form of the fault is determined by its roughness. Under stress-driven condition, a rougher fault slips more stably, while a smoother fault shows a sudden and rapid slip. During fluid injection, all the faults with different roughnesses showed stick-slip phenomenon. Obviously, the mechanisms of fault instability in the two methods are substantially different. In addition, the uneven distribution characteristic of pore pressure depending on permeability differences resulted in a higher pore pressure required for fault instability than the predicted pore pressure by Mohr-Coulomb criterion. This study revealed the mechanisms of stress- and fluid-pressure-driven fault reactivation, and explain the influence of roughness and permeability of faults on injection-induced earthquakes.

1 Introduction

Fluid injection is a preferred method for the stimulation of Enhanced Geothermal Systems (EGS) to elevate permeability from micro- to milli-Darcy levels. Fluid injection-induced reductions in effective stress are capable of reactivating fractures in brittle failure. The key is to generate permeability through shear reactivation but avoid creating runaway slip that can trigger large seismic events (Lengliné et al., 2017). Since 2019, China has initiated its first EGS development project in the Gonghe basin on the northeastern extent of the Tibetan plateau (Zhang et al., 2022). The northeastern part of the Qinghai–Tibet Plateau is a tectonically active area with a high risk of strong earthquakes. In 1990, an Mw 6.4 earthquake occurred ~30 km from the Gonghe EGS site (Hao et al., 2012). The Gonghe EGS is in a still higher stress environment with a further elevated risk of injection-induced seismicity. Controls on fluid injection induced seismicity on variable roughness faults under non-stationary and strongly heterogeneous distributions of pore fluid pressures remain unclear. To address this issue, we complete experiments and analytical characterizations on laboratory faults under various total stress and fluid pressure stress paths.

Characterizations of fault friction based on constant friction (Jaeger et al., 2009) are unable to replicate stick-slip phenomena observed during earthquakes. Rate- or velocity-weakening response is a necessary requirement (Scholz et al., 1972; Dieterich, 1978) to replicate this behavior. Slip weakening may be defined over a slip weakening distance (Palmer and Rice, 1973) and as a function of state (Dieterich, 1979). These relations usually define the evolution of second-order frictional effects under prescribed velocity conditions and under constant effective stress - but stress paths are rarely simple and fluid injection reactivations can be strongly varying in both space and time.

Injection-induced earthquakes are impacted by the minimum principal stress (Maurer & Segall, 2018), the total volume of injected fluid (Galis et al., 2017) or related to Gutenberg-Richard statistics (van der Elst et al., 2016; Yu et al., 2022). These models assume that pore pressure is uniformly distributed during fluid injection, but laboratory tests and field studies show that the fluid pressure required to activate a fault is often higher than that predicted using the Mohr–Coulomb failure criterion. An uneven diffusion of fault overpressure substantially affects the stress field and fault stability. The overpressure distribution (Ji et al., 2020, 2021), together with the heterogeneous diffusion of pore pressure (Passelègue et al.,2018; Ishibashi et al., 2018; Wang et al., 2020) impact fault instability driven by injection. During the injection, the distribution of pore

pressure in a fault is influenced by various factors such as fault roughness, in-situ stress state, mineral composition, and injection conditions (Fang & Wu, 2022). These factors are implicit in defining the heterogeneous permeability of faults and thereby the uneven distribution of pore pressure.

At present, several experimental methods have been developed to simulate the frictional slip on rock faults. According to the characteristics of loading, they can be divided into single direct shear, double direct shear, rotary shear, and triaxial shear testing configurations. Single direct shearing is conducted by fixing the lower fault and applying normal and shear loads to the upper block (Zhao et al., 2018a, b). This method has simple stress boundary conditions, but the load distribution on the fault surface is not uniform due to its loading characteristics. Double direct shearing uses three blocks with two parallel fault interfaces to apply a near uniform and moment-free shear stress to two fault surfaces (Collettini, 2014). This enables a more uniform distribution of shear load on the fault surface. Under rotary shear (Ujiie & Tsutsumi, 2010; Cornelio et al., 2019), the shear stress is applied by fixing the upper/lower part of a toroidal rock sample and rotating the lower/upper part around a central axis under applied normal stress. This method can represent both high shear rates and large shear displacements. However, rotary shear has difficulty in applying large excess pore pressures to the fault. Triaxial shear tests allow inclined faults traversing a cylindrical sample to be reactivated (Wu et al., 2017; Ye & Ghassemi, 2018). Cylindrical rock samples containing 45° to 60° prefabricated fractures are used to concurrently apply normal and shear stress to the laboratory fault *via* confining pressure and axial stress. Triaxial shear tests allow control of the ratio of normal to shear stress through the selection of fault angle as a complex stress together with the ready application of temperature and pore pressures.

To address the mechanism of stress- and fluid-pressure-driven instability of various roughness faults we complete experiments and analytical characterizations on laboratory faults under various total stress and fluid pressure stress paths. The mechanical (stress and displacement) and transport characteristics (pore pressure and permeability) of faults with different surface roughness were characterized to constrain frictional slip under both total stress- and fluid-pressure-driven stress paths. Finally, we discuss the effect of fault roughness and permeability on injection-induced earthquakes to improve our ability to assess and mitigate the risk of anthropogenic earthquakes in EGS.

2 Materials and Methods

The granites used in this study are surface outcrop derived samples of granites from the Gonghe basin, Qinghai Province, China. These granites are 37% quartz, 33% microplagioclase, 25% mica, 3% amphibole, and 2% plagioclase (Chen et al., 2020) by volume. The resulting cylindrical samples are 50 mm in diameter and 100 mm in height and contain a diamond sawcut fault inclined at 45° and pierced by two 1.5-mm-diameter boreholes accessing pressurized fluids from the end platens. The boreholes were used to change pressures and therefore effective stresses and also to measure permeability before and after slip. The fault surfaces are roughened with sandpaper corresponding to particle sizes of 150 μm, 23 μm, and 1.3 μm, for different fault roughnesses. A Top Industrie high-temperature triaxial testing system was used to conduct the reactivation experiments. The maximum axial load of the system is 1500 kN with confining pressures and pore pressures in the range 0–60 MPa. Silicon oil is used as the confining fluid. The sample and test configuration are shown in Figure 1.

Nine rock samples were produced from the same surface outcrop sample with the cylindrical samples divided into three groups according to the variable roughnesses of the fault surfaces. Sample information is shown in Table 1.

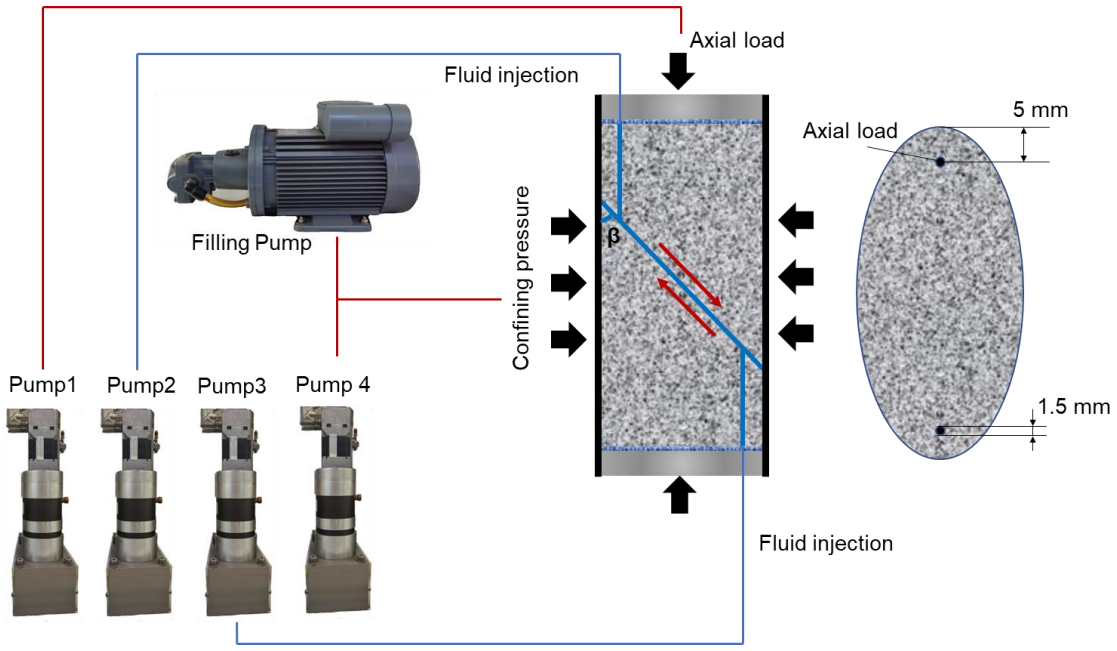

Figure 1. Schematic of rock sample and testing configuration. Four pumps separately regulate the axial pressure, confining pressure and the pore pressure at both ends of the sample.

Each test consists of two separate stress paths: stress-driven frictional slip followed by fluid-pressure-driven frictional slip. Specific test procedures are described as follows:

Step 1: Initial state. The sample was vacuum saturated with deionized water and then sealed by polyurethane sleeves before hydrostatic loading ($\sigma_1 = \sigma_2 = \sigma_3$). Previous research has shown that the friction coefficients of fault in rock decrease as a result of pore water presence (Byerlee, 1967). In order to ensure that the fault is always saturated during the test, a pore pressure of 1 MPa was then applied to saturate the fault before being reduced to 0.5 MPa. Fault permeability was measured for steady state flow (Brace et al., 1968) with an upstream (1.5 MPa) to downstream (0.5 MPa) pore pressure differential of 1 MPa.

Step 2: Stress-driven fault activation. We selected constant stress as a load target in order to ensure that faults with different roughness are at the same stress level before injection. Axial stress targets were larger than the reactivation stress of the fault and increased with the confining pressure. Axial stress was applied at 0.01 MPa/s according to the experimental schedule of Table 1. This results in normal and shear stresses increasing simultaneously on the fault with the rate of shear stress increase greater than that of the normal stress. When the shear stress exceeds the maximum frictional strength the fault, the fault slips and the static frictional strength was recorded to calculate the coefficient of friction. Subsequently, the fault went through the initial run-in stage until the axial stress retained constant. Fault permeability was measured using the method of Step 1.

Step 3: Fluid-pressure-driven fault reactivation. Deionized water was injected into both boreholes simultaneously at a rate of 0.05 cm^3/min after the fault reached steady state. The increase in pore pressure leads to a decrease in effective normal stress and the reactivation of fault slip – that reactivation pore pressure is recorded. The pore pressure continues to increase to 50% of the confining pressure after reactivation. Then, the outlet pore pressure was retained constant and the inlet pore pressure increased by 1 MPa with the fault permeability measured as above.

The axial force applied to the sample is usually measured using a load cell located outside the pressure vessel. In this case, however, part of the measured force is resisted by the friction between the moving piston and the confining sealing assembly (Tembe et.al, 2010). Therefore, a load cell was located inside the confining pressure vessel to measure true axial force applied to the sample.

The axial force was also corrected by considering and calibrating out jacket restraint during the tests (Ji, 2020).

The axial displacement (Δl) can be obtained from a linear variable displacement transducer (LVDT) installed on the sample. The fault slip displacement (u) can therefore be estimated as,

$$u = (\Delta l - \frac{\sigma_1 \cdot l}{E}) \cdot \frac{1}{\cos \beta} \quad (1)$$

where β is the dip angle of the fault surface (in our case, β=45°), E is the Young's modulus of the granite, σ_1 is axial stress and l is the length of the cylindrical sample. In this study, axial stress σ_1 is computed by dividing the uncorrected stress by the factor A/A_0,

$$A / A_0 = (\theta - \sin \theta) / \pi \quad (2)$$

$$\theta = \pi - 2\sin^{-1}\left[(u / dr)\tan \beta\right] \quad (3)$$

where θ is the angle subtended by the points of intersection of two overlapping circles. At the centers of the circles, A_0 and A are the original and corrected cross-sectional areas of the sample. In this study, the maximum fault shear displacement does not exceed 2mm, and the area correction results in a stress adjustment of 3.59% at 2mm.

The normal stress and shear stress on the fault surface in the center of the sample were calculated from the axial stress σ_1 and confining pressure σ_3 as:

$$\tau = \frac{1}{2}(\sigma_1 - \sigma_3)\sin 2\beta = (\sigma_1 - \sigma_3)\sin \beta \cos \beta \quad (4)$$

$$\sigma_n = \frac{1}{2}\left[(\sigma_1 + \sigma_3) - (\sigma_1 + \sigma_3)\cos 2\beta\right] = \sigma_3 + (\sigma_1 - \sigma_3)\sin^2 \beta \quad (5)$$

The aperture used to calculate permeability was determined from the cubic law.

$$Q = \frac{g}{\nu}\frac{we^3}{12} J \quad (6)$$

where Q is the volumetric flow rate within the fracture, w is the width of the cross-sectional area of flow between parallel plates, v is the kinematic viscosity of the fluid, g is the gravitational acceleration and J is the hydraulic gradient of unity. By measuring the flow rate of the fault, the equivalent hydraulic aperture e_h can be determined. Combined with Darcy's law, the permeability k of the fracture can be obtained from

$$k = \frac{e_h^{\,2}}{12} \tag{7}$$

All data are acquired in real-time at a sampling rate of 10 Hz with fault roughness measured by a 3D laser scanner both pre- and post-test to define evolving damage characteristics of the fault surface during the reactivation.

Table 1. Rock sample characteristics and experiment matrix.

Sample Number	Size of sandpaper (μm)	Confining pressure (MPa)	Axial stress (MPa)	Load rate (MPa/s)	Injection rate (mL/s)
1-1	150	10	34	0.01	0.05
1-2	150	20	68	0.01	0.05
1-3	150	40	136	0.01	0.05
2-1	23	10	34	0.01	0.05
2-2	23	20	68	0.01	0.05
2-3	23	40	136	0.01	0.05
3-1	1.3	10	34	0.01	0.05
3-2	1.3	20	68	0.01	0.05
3-3	1.3	40	136	0.01	0.05

3 Experimental Result

3.1 Fault slip characteristics

The shear stress on the fault is normally obtained by a displacement-driven shear test which is carried out at an axial displacement rate (Ji & Wu, 2020). However, this method can only estimate the shear stress of fault at steady state slip, without accurately estimating the slip point and the change of friction coefficient in the initial run-in period under stress-drive. In order to obtain the intact slip characteristics of the fault under stress-drive, we use a constant loading rate instead of a constant displacement rate. Figures 2a-2c show the stress/pressure/displacement versus time behavior under stress- and then fluid-pressure-driven reactivation (using a representative example at a confining pressure of 20 MPa with all other results catalogued in the supporting information S1). In stress-driven fault activation, the stable stage in which shear displacement does not increase on a fault can be observed clearly. As the axial stress continues to increase, the fault slips at a constant shear rate after an acceleration. At this time, the fault enters the steady-state initial condition after the initial run-in period.

Subsequently, the faults with varied roughness showed different reactivation characteristics under stress-driven conditions. For the roughest fault (roughened at 150 μm; Figure 2a), the fault reactivated with stable-slip that arrested when the axial loading was stopped. For the medium-

roughness fault (roughened as 23 μm; Figure 2b) a small stress drop occurred after reactivation before stable slip resumes. Finally, the smoothest fault (a particle size of 1.3 μm; Figure 2c) reactivates in stick-slip with a large stress drop and shear displacement and accompanied by an audible noise. Multiple stick-slips followed until the axial stress remained stable after the fault slip stopped. In addition, the peak stress in rock sample 3-3 was limited by repeated stick-slip. Therefore, a liquid injection-induced slip test was carried out while keeping the axial stress at 100 MPa.

Following the stress-driven reactivations, the samples were again reactivated by fluid pressures – and again reactivated in contrasting styles according to fault roughness. For smooth rock samples, a continuous stick-slip phenomenon occurred during the fluid injection.

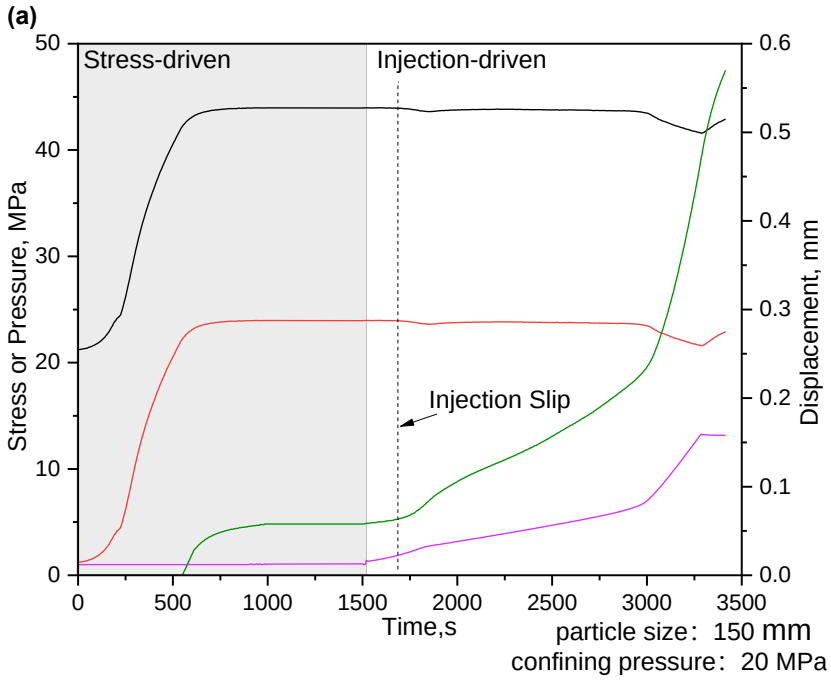

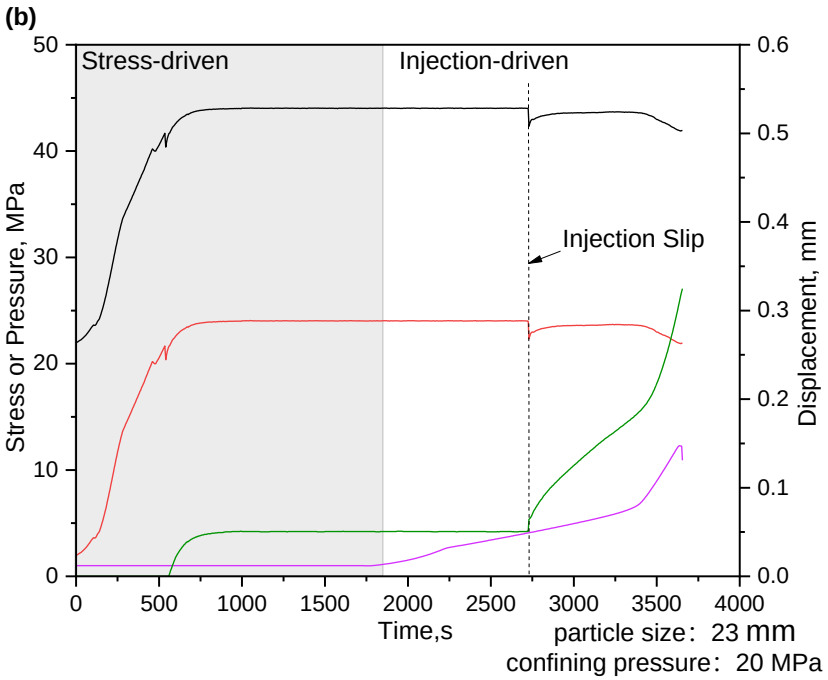

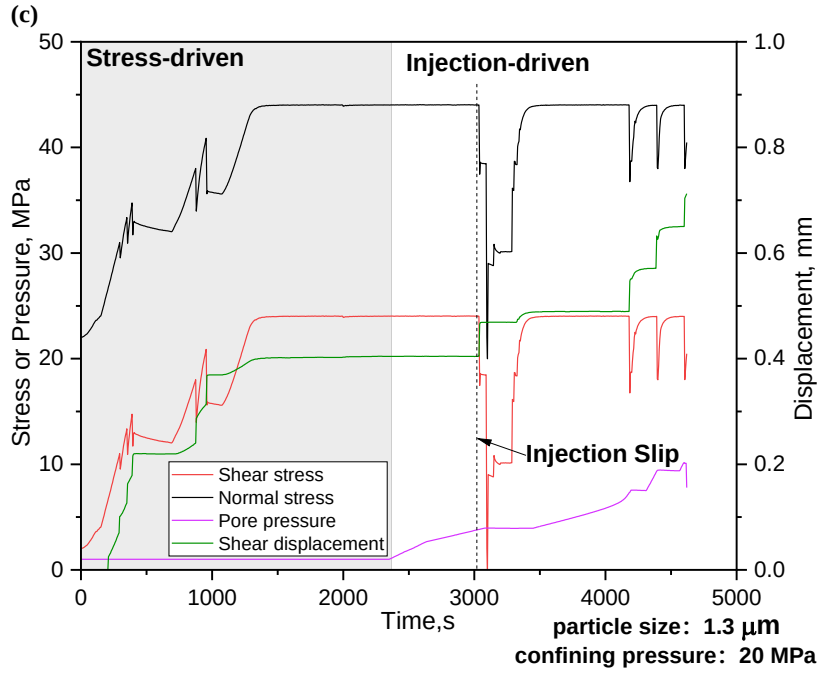

Figure 2. Stress, displacement, and pore pressure histories for the stress- and fluid-pressure-driven reactivation experiments: (a) Rough sample 1-2, (b) Intermediate roughness sample 2-2, and (c) smooth sample 3-2. The first half of the time history is under stress-driven conditions and the second half under fluid-pressure-driven conditions.

The effective normal stress σ_{en} on the fault surface is equal to the difference between the normal stress σ_n and pore pressure P_W as:

$$\sigma_{en} = \sigma_n - P_w \tag{8}$$

Figure 3 shows the Mohr-Coulmb failure envelopes for the faults during stress-driven and fluid-pressure-driven reactivations. We construct the failure envelopes for the faults by fitting the shear strengths obtained from the stress-driven frictional slip experiment, and derive the maximum static friction coefficients for the faults polished by 150 μm, 23 μm, and 1.3 μm grit sandpapers as 0.53, 0.50, and 0.24, respectively. The shear stress on the faults gradually increased and then remained constant after axial loading was stopped. Fluid was then injected into the fault at a constant injection rate and the effective normal stress reduced. Although the fault was already critically stressed, the fault does not reactivate until its stress state reaches a new envelope (blue dashed line). The pore pressure measured from the injection boreholes is thus larger than that predicted by the failure criterion. This is similar to the overpressure phenomenon found in other experiments and field studies (Kakurina et al., 2019; Rutter & Hackston, 2017; Cappa et al., 2019) representing a higher reactivation friction coefficient for fluid injection versus a change in total stress.

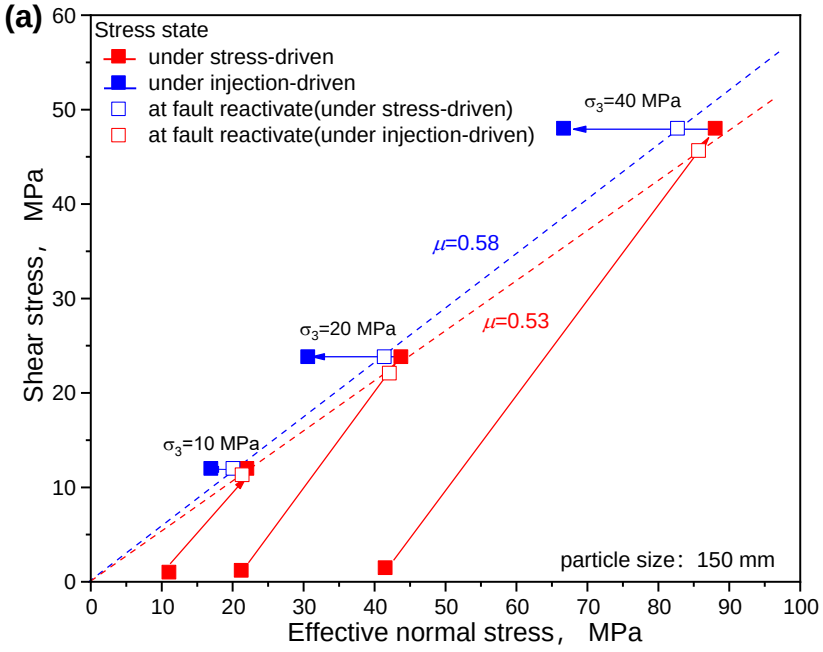

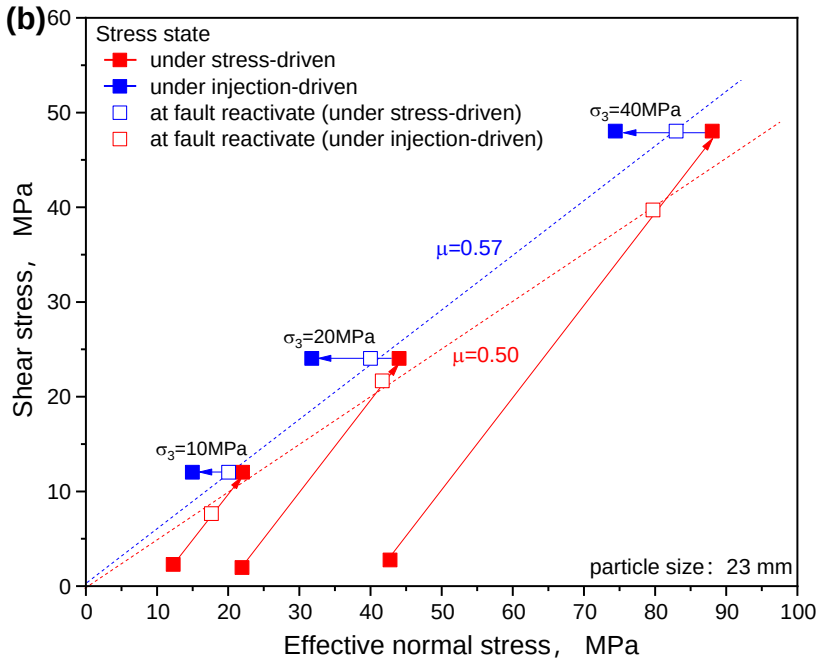

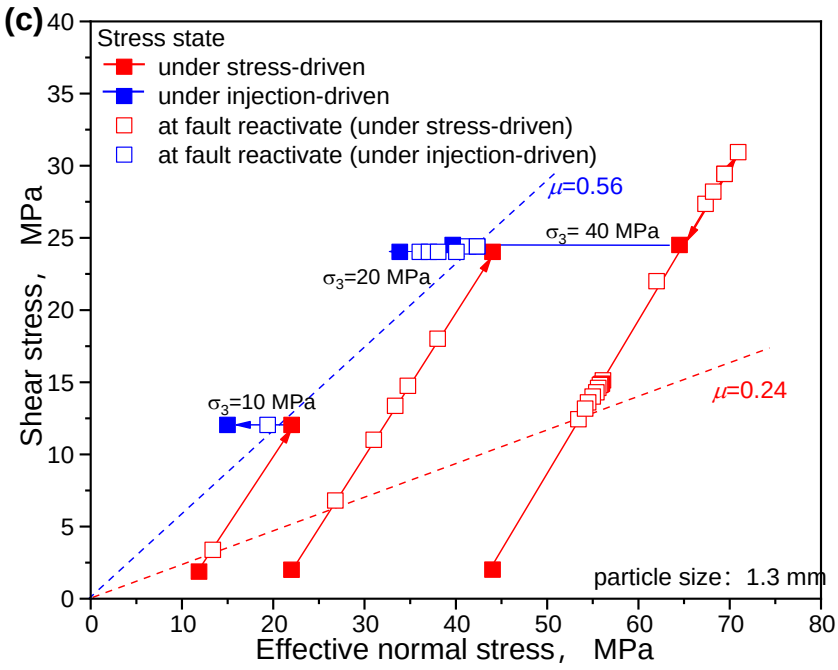

Figure 3. Mohr-Coulmb failure envelopes for laboratory faults reactivated by stress- and fluid-pressure-driven: (a) Samples polished to 150 μm roughness under confining pressures of 10 MPa, 20 MPa, and 40 MPa; (b) Samples polished to 23 μm roughness under confining pressures of 10 MPa, 20 MPa, and 40 MPa; (c) Samples polished to 1.3 μm roughness under confining pressures of 10 MPa, 20 MPa, and 40 MPa.

3.2 Fault damage characteristics

A three-dimensional (3-D) laser scanning system, with a 10-μm resolution laser beam, was used to measure the topography of the fault surfaces. Typical profiles of the fault surface both before and then after slip are shown in Figure 4. The main signature of the reactivation deformation is striations as damage along the slip direction. After the test, the fault surface was observed by microscope and no wear products were present on the fault surface. This is consistent with the phenomena observed in previous studies (Ye and Ghassemi, 2018; Bijay and Ghazanfari, 2021; Vogler et al., 2016). In this case, the smooth saw-cut fault does not develop a significant gouge layer during the reactivation. The fault surface only produces a small amount of damage as concave striations.

The volume of the concave striations on the fault surface caused by the damage was used to characterize the damage on the fault surface during slip (Zhao et al., 2018b). This is equivalent to the height and the area of the concave striations. The damage volume of each fault (shown in Table 2) is minute as compared to rough natural faults (Ji & Wu, 2020). This indicates that the surface damage of the sawcut fault used in this work is much less than that of natural faults.

Fault slip characteristics are also affected by the uneven distribution of fault surface roughness (Cappa et al., 2022). The roughness of the fault surface is uniformly distributed before the test. However, it is possible to reorganize the distribution of roughness during slip due to the uneven distribution of damage. We use the standard deviation of fault damage depth to characterize the heterogeneity of fault damage (shown in Table 2). The standard deviation of each rock sample is small, at 0.04~0.07 μm, indicating that the damage distribution on the fault surface is relatively uniform.

For these reasons, the influence of fault gouge and the uneven distribution of fault surface roughness caused by wear is neglected in the discussion that follows.

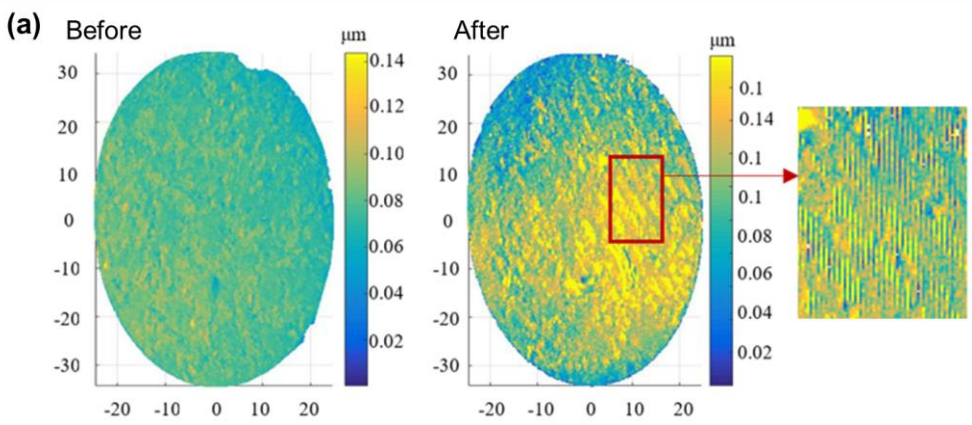

Figure 4. Damage on fault surfaces during reactivation: (a) Typical scanning results of a fracture surface.

Table 2. The standard deviation of damage on fractured rock samples.

Sample number	Confining pressure（MPa）	Damage standard deviation（μm）			Volume of damage（mm^3）
		A	B	Average	
1-1	10	0.0482	0.0441	0.04615	2.711
1-2	20	0.0408	0.0474	0.0441	2.729
1-3	40	0.0497	0.0561	0.0529	2.769
2-1	10	0.0469	0.0429	0.0449	2.748
2-2	20	0.0417	0.0409	0.0413	2.762
2-3	40	0.0444	0.0616	0.053	2.788
3-1	10	0.0536	0.0511	0.05235	2.641
3-2	20	0.0495	0.0487	0.0491	2.665
3-3	40	0.049	0.0672	0.0581	2.695

3.3 Fault permeability characteristics

Fault slip reactivation may substantially affect the aperture of faults and hence permeability. Permeability may change in sense depending on the mineral composition, stress conditions, surface roughness, and shear displacement of the rock (Fang & Wu, 2022). Fault permeability also influences the rate of pore pressure diffusion within the fault. In this study, the permeability of faults has been measured from the initial state, after both stress-driven fault reactivation and then after fluid-pressure-driven fault reactivation, respectively. These results are catalogued in the supporting information S3. To obtain the evolution of permeability under fault reactivation, the fault permeability and shear displacements were normalized with respect to the initial permeability and maximum shear displacement following reactivation.

Figure 5 shows the normalized permeability and the normalized shear displacement of the various faults after stress-driven reactivation. The fault permeability decreases with an increase in shear displacement as a result of fault compaction under stress-drive (Ishibashi et al., 2018; Jia et al., 2020; Fang & Wu, 2022). For a natural rough fault, the evolution of asperity geometry and distribution modifies the fracture aperture and the flow velocity and subsequently enhancement the fault permeability (Ye and Ghassemi, 2018). However, the smooth fault surfaces in this study cannot drive significant fracture dilation. The fault damage characteristics noted in Section 3.2, representing shallow striations of damage on the fault surface, do not promote significant shear dilatancy.

The fault permeability increased under fluid-pressure-driven. This is opposite to the trend in permeability change under stress-driven condition. In this condition, the major contributor to permeability enhancement is the normal dilation resulting from the increase of pore pressure in fault. The permeability enhancement during fracture shearing is highly dependent on fault roughness and stress state (Ye and Ghassemi, 2018). For a low-roughness fault at high stress, a rapid slip with an associated large stress drop is induced under injection-driven reactivation, creating a much larger increase in fracture permeability. This results in a significant increase in the permeability of smooth faults, up to 36 times higher than the initial permeability (Figure 5c).

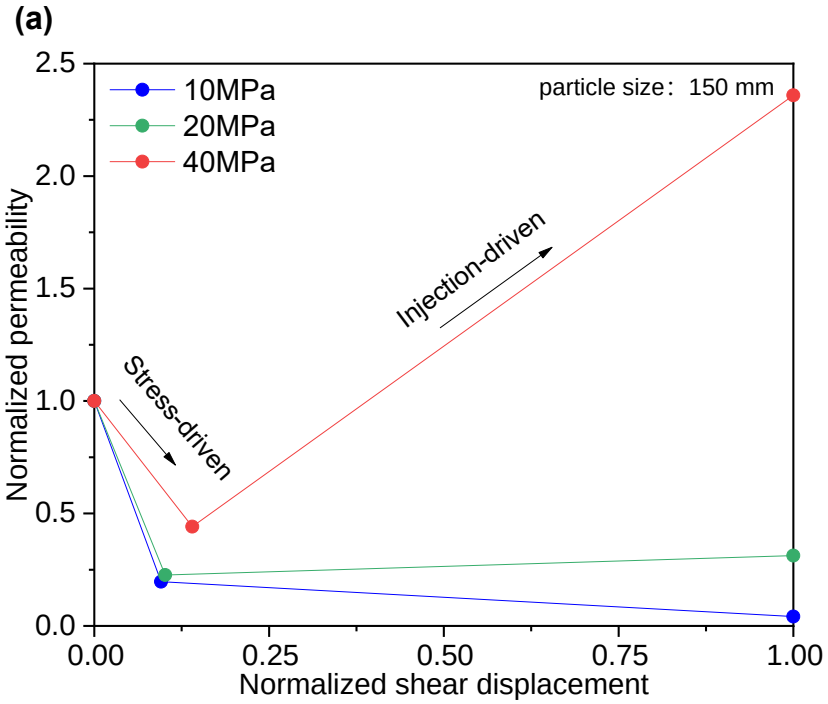

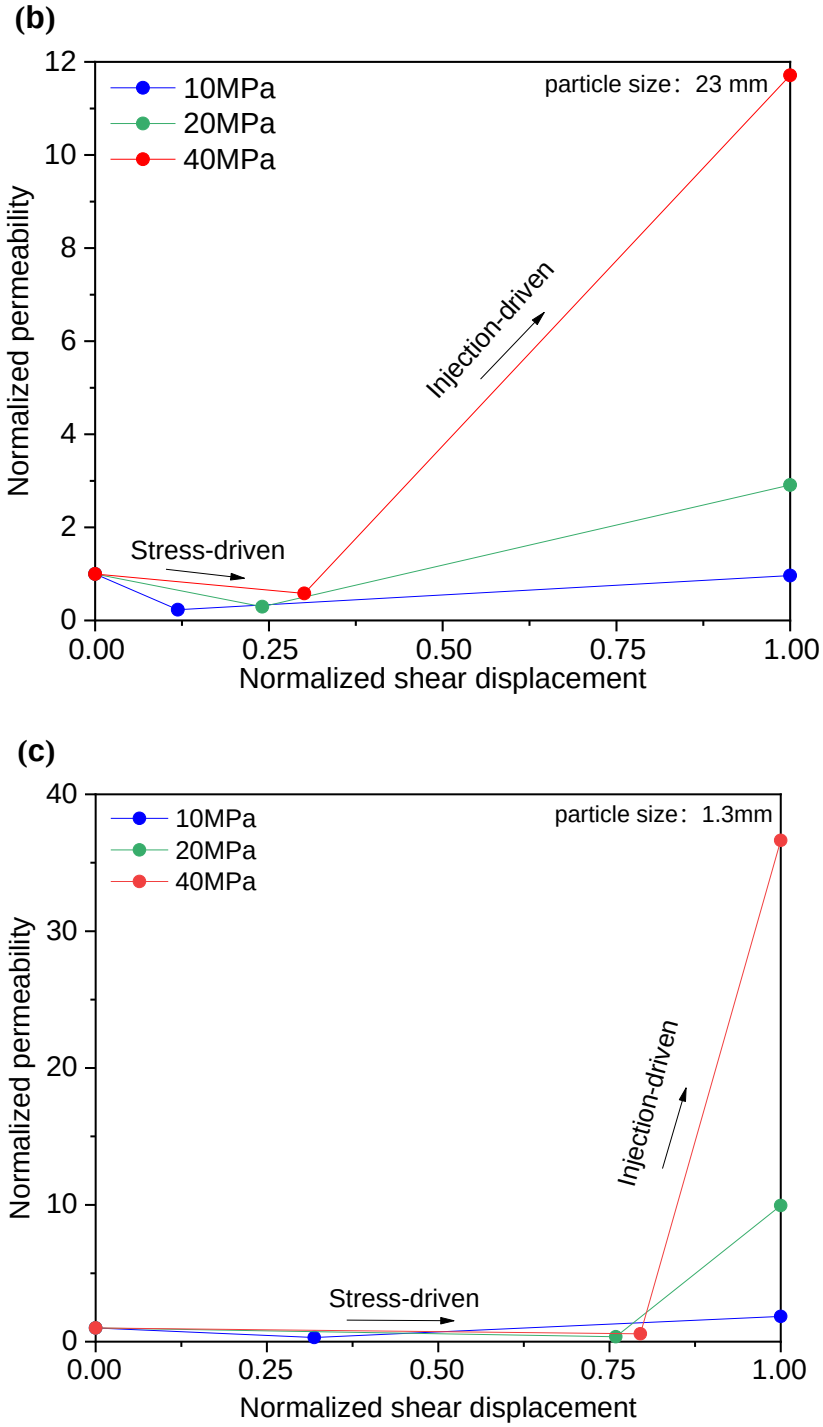

Figure 5. Normalized fracture permeability as a function of normalized shear displacement: (a) Samples polished to 150 μm roughness under confining pressures of 10 MPa, 20 MPa, and 40 MPa; (b) Samples polished to 23 μm roughness under confining pressures of 10 MPa, 20 MPa, and 40 MPa; (c) Samples polished to 1.3 μm roughness under confining pressures of 10 MPa, 20 MPa, and 40 MPa.

4 Discussion

4.1 Mechanism of fault activation under stress-drive conditions

The mechanism of fault slip under stress-drive conditions may be explored by investigating the evolution of mechanical properties (shear and normal stress, shear displacement, friction coefficient and shear velocity). It is suggested that data sampled at less than 10 Hz may underestimate the values of the dynamic slip events (McLaskey & Yamashita, 2017; Passelègue et al., 2019). Therefore, we will not discuss the rate of fault slip. In Figure 6, The friction coefficient is obtained by the ratio of shear stress to normal stress. Three stages of fault reactivation can be defined under stress-drive conditions according to the evolution of shear displacement:

(1) Stability stage: The shear displacement is kept at zero during the stress loading. The shear stress remains below that of static friction and the fault remains stable.

(2) Initial slip stage: Shear stress exceeds the peak static friction and shear displacement begins to increase. The shear displacement increases linearly with the shear stress after an acceleration. At this time, the fault enters a steady-state initial condition after the initial run-in period.

(3) Continuous slip stage: As the axial stress continues to increase, high roughness faults (Figure 6a, using a representative example of sample 1-3 with all other results catalogued in the supporting information S1) remain in stable-slip and the friction coefficient increases with slip. For a smooth fault, the fault reactivates in stick-slip with a stress drop and shear displacement. The friction coefficient changes from the maximum static friction coefficient to the dynamic friction coefficient during this period. With an increase in the normal stress and shear stress, the friction coefficient gradually increases until the loading stops or the next stick-slip occurs.

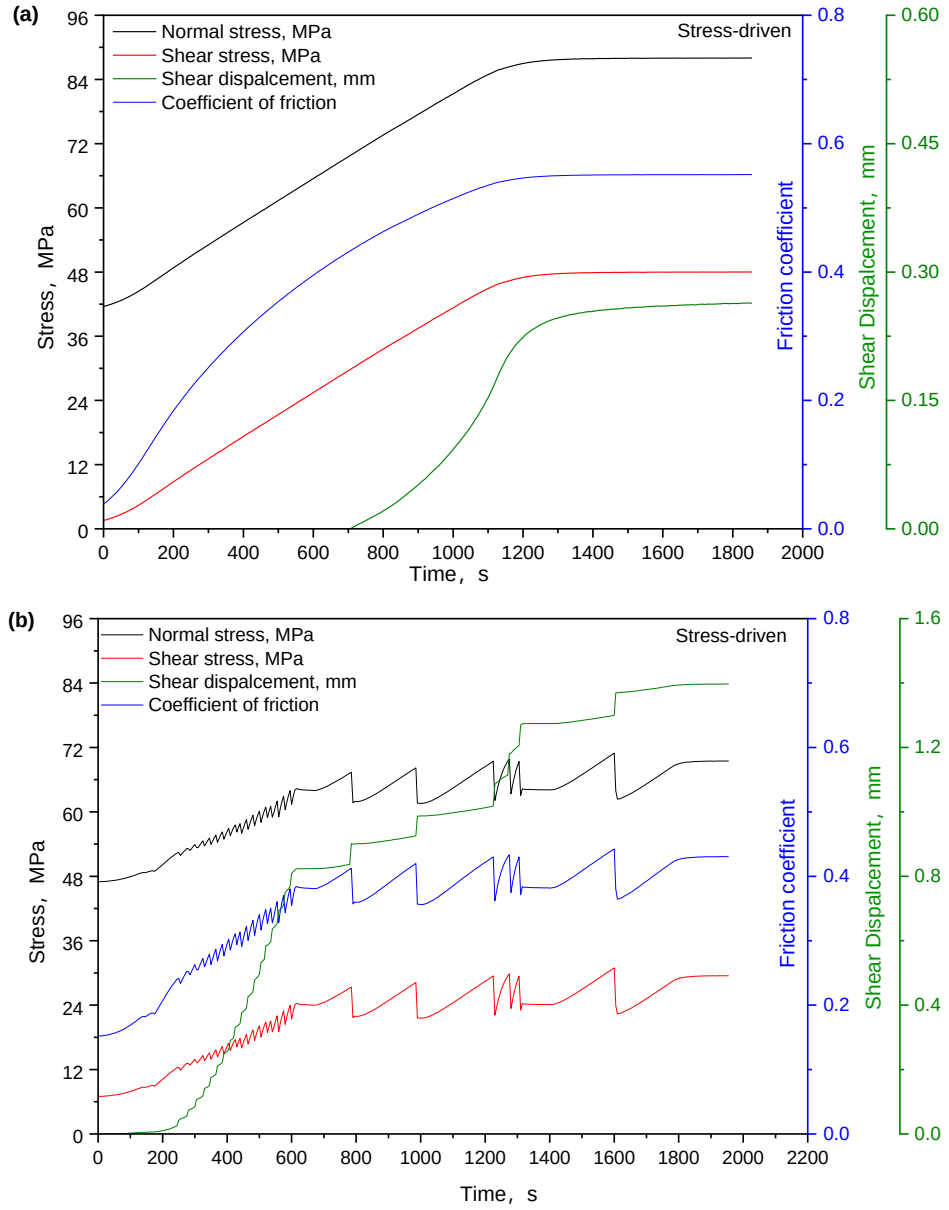

Figure 6. Change in mechanical properties during stress-driven frictional slip: (a) Stable-slip; (b) Stick-slip.

According to the three stages of fault slip, the change in friction coefficient is related to the fault stress state, slip distance, and slip characteristics (stable-slip or stick-slip) during continuous stress loading. At present, the four most widely used models to describe fault slip are rate weakening (Tsutsumi and Shimamoto, 1997), rate- and state-dependent models with either an aging law (Dieterich, 1978) or slip law (Ruina, 1983), and slip weakening friction (Ida, 1972). Among them, the first three require rate data during slip. These data are difficult to recover for practical engineering applications. According to the friction law related to slip weakening, the change in

355 friction coefficient with slip shows a linear or nonlinear relationship. The friction relationship for
356 slip weakening under linear conditions can be described as (Ida, 1972):

357
$$\tau = \begin{cases} \left[\mu_s - \left(\mu_s - \mu_f\right)\frac{u}{d_0}\right]\sigma_n & ,u < d_0 \\ \mu_f \sigma_n & ,u \geq d_0 \end{cases} \tag{9}$$

358 where μ_f and μ_s are the maximum dynamic friction coefficient and static friction coefficient,
359 respectively; u is the relative slip displacement between upper and lower fault surfaces; σ_n is the
360 normal stress on the fault surface; d_0 is the characteristic slip distance, representing the slip distance
361 required for the static friction coefficient to decrease to the dynamic friction coefficient.
362 Therefore, the analysis of friction slip mechanism of faults under stress-driven condition can be
363 described as follows: As shown in Figure 7a, the transition from the initially stable stage to slip
364 can be explained by the Mohr-Coulmb failure criterion. Fault slip occurs when the shear stress on
365 the fault exceeds its maximum static frictional resistance. Faults with a high roughness faults
366 mainly return stable slip (Figure 7b). In this circumstance, the maximum static friction coefficient
367 of the fault μ_s and dynamic friction coefficient μ_f are equal. Thus, Eq. (9) becomes
368
$$\tau = \mu_f \sigma_n = \mu_s \sigma_n \tag{10}$$

369 Considering the influence of fault angle, substituting Eqs. (4) and (5) into Eq. (10) yields,

370
$$\mu_s = \mu_f = \frac{\tau}{\sigma_n} = \frac{\left(\sigma_1 - \sigma_3\right)\cos\beta\sin\beta}{\sigma_1 \sin^2\beta - \sigma_3 \cos^2\beta} \tag{11}$$

371 It is apparent from Eq. (11) that in the fault strengthening stage, the fault friction coefficient is
372 mainly related to the stress level and the angle of fault surface. As shown in Figure 7c, the fault
373 slips by shear offset d_1 at the onset of the first stick-slip event. The stress drop on the fault surface
374 changes according to the difference in the static friction coefficient μ_{s1} to the dynamic friction
375 coefficient μ_{f1}. The frictional slip characteristics of the fault surface still conform to Eq. (9). Then,
376 as the stress continues to increase, the fault strengthens and the friction coefficient gradually
377 increases. At this time, the fault slips stably, which conforms to Eqs. (10) and (11). During fault
378 slip, the maximum static friction coefficient changes from μ_{S1} to μ_{s2}. When the fault friction
379 coefficient grows to a new maximum static friction coefficient μ_{s1} during the fault strengthening,
380 the fault becomes stick-slips again. This cycle is repeated until the loading stops.

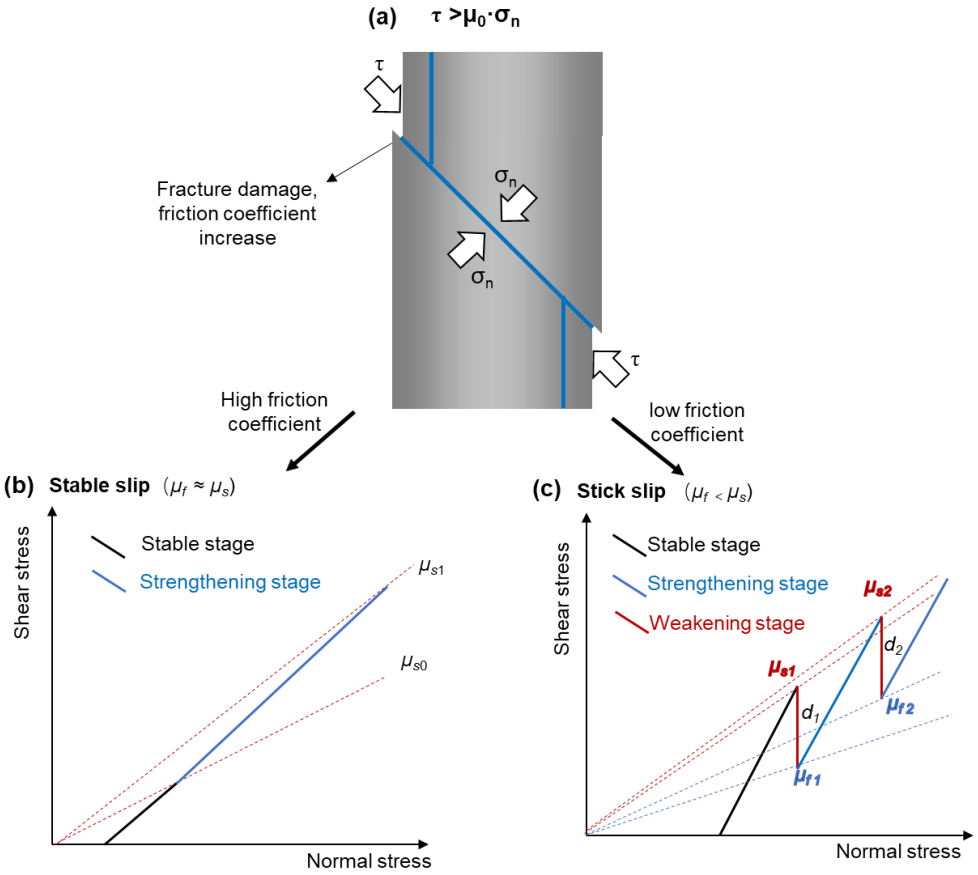

Figure 7. Mechanisms of fault reactivation under stress-driven: (a) Schematic of fault instability; (b) Stable slip under stress-driven conditions; (c) Stick-slip under stress-driven conditions.

Therefore, the slip-weakening law under linear conditions may be modified and the slip-weakening law during fault strengthening and continuous stick-slip proposed as:

$$\tau = \begin{cases} \left[\mu_{si} - \left(\mu_{si} - \mu_{fi}\right)\dfrac{u}{d_i}\right]\sigma_n & D_i < u < D_i + d_i \\ \dfrac{\left(\sigma_1 - \sigma_3\right)\cos\beta\sin\beta}{\sigma_1\sin^2\beta - \sigma_3\cos^2\beta}\sigma_n & d_i < u < D_{i+1} \end{cases} \tag{12}$$

where i is the stick-slip event sequence number, d_i is the slip distance required for friction to drop from static to dynamic for the ith stick-slip, $\mu_{si,}$ and μ_{fi} are the static friction coefficient and the dynamic friction coefficient for the ith stick-slip, and D_i is the length of fault slip before the ith stick-slip. When the fault is in its stable slip stage, the characteristic slip distance of the fault d_i = 0, and Eq. (12) returns Eq. (11). Therefore, Eq. (12) can characterize both stable slip and stick-slip events.

In addition, when using Eq. (12) to calculate frictional slip, it is necessary to obtain the characteristic slip length d_i. In stick slip, the slip distance of the fracture is often related to the difference in the stress on the fracture surface from before until after slip (Mohammadioun, 2001). The stress drop is calculated as:

$$\Delta\sigma=\sigma_0-\sigma_1 \quad (13)$$

If the stress drop distribution of historical earthquakes is known, then the dynamic process of earthquake rupture may be illuminated. The characteristic slip length d_i increases with the stress drop. Because of the non-uniform distribution of stress and strength near the fault, the relationship between slip distance and stress drop is generally complex. Two methods are primarily used to evaluate stress drop. The first is to apply a scaling relationship based on comparing the earthquake magnitude with its radiated energy or the estimated fault rupture area (Andrews, 2013). The second is to estimate the stress drop by finding the relevant parameters in the model through a source spectrum analysis based on an assumed source model. Where the source spectrum analysis is used, a disc fault model is generally assumed for small and medium-sized earthquakes. Here, a disk of radius R, is subject to a stress drop $\Delta\sigma$ as

$$\Delta\sigma=\frac{7}{16}\cdot\frac{M_0}{R^3} \quad (14)$$

where M_0 is the seismic moment. This moment may be evaluated from the shear modulus G of the fractured rock mass (Aki, 1966) as,

$$M_0 = GSd \quad (15)$$

where, S is the area of the fault, m^2. G can be considered as the combined rigidity of the test system and the fracture and can be determined based on the least squares method to achieve the minimum value of the sum of squared residuals (Ji et al. 2019):

$$G=\frac{M_0\sum_{i=1}^{n}d_i}{S\sum_{i=1}^{n}(d_i^2)} \quad (16)$$

Figure 8 shows the relationship between slip distance and stress drop during the stick-slip cycle. The trends of stress drop and slip displacement remain the same under both stress- and injection-drive. The combined rigidity is recovered from the least squares method and results in a best-fit value of 0.55 GPa (R^2=0.90). The fitting results agree well with the stress drop and slip displacement measured directly in the tests, indicating that the derived rigidity is reasonable. By

monitoring the magnitude of the stress drop on the fault surface, the characteristic slip value d_i can be obtained, and the entire fault slip process followed.

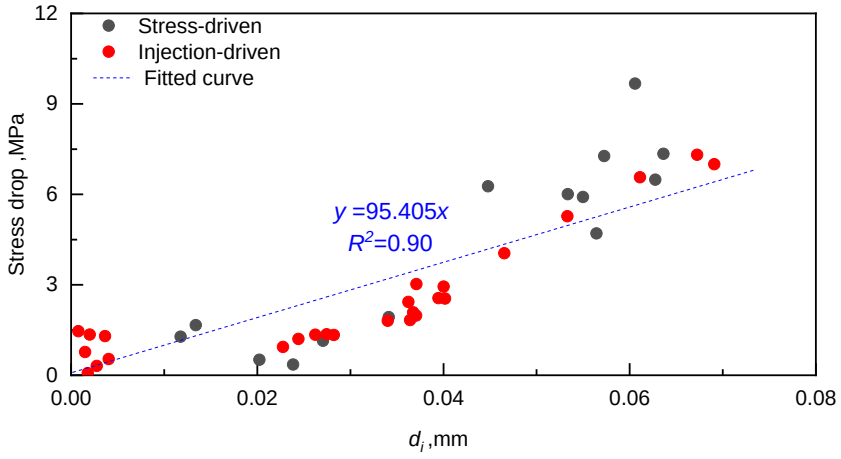

Figure 8. Stress drop with slip distance. Black points are the experimental data under stress-drive; Red points are the experimental data under injection-drive. The blue dotted line is obtained by jointly fitting the experimental data under stress-drive and injection-drive.

4.2 Mechanism of fault reactivation under fluid-pressure-driven condition

Figure 9 shows typical slip distance versus friction coefficient results for stable slip and stick–slip processes. Frictional slip under fluid-pressure-drive can also be divided into three stages: a stable stage, an initial slip stage then a continuous slip stage, similar to the slip characteristics under stress-drive. In the stable stage, despite the increase in pore pressure, the fault does not slip. In the initial slip stage, when the pore pressure increases to a threshold, the fault shows stick–slip. In the continuous slip stage, and with the continued fluid injection, the fracture stick-slips several times and this remains the predominant mode of slip.

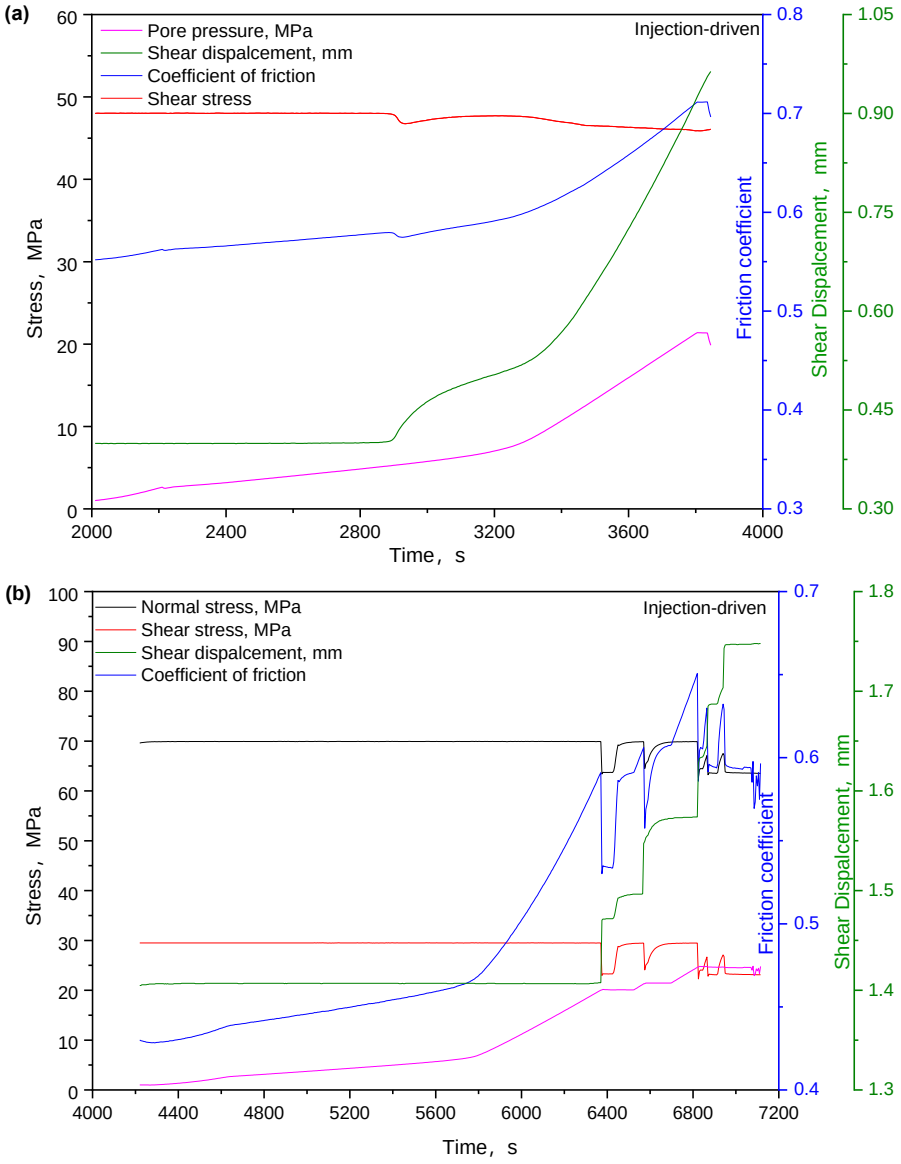

Figure 9. Evolution of mechanical properties under injection-drive: (a) Smooth fault; (b) Rough fault.

The faults in the pressure-drive tests have already slipped in the preceding stress-drive portion of the test. The faults did not slip during the stable stage of fluid injection, indicating that the pore pressure in the fault injection borehole is higher than the pore pressure predicted by the Mohr-Coulmb failure criterion. An overpressure ratio (Ji et al., 2021) may be defined as the ratio of fluid pressure increase measured at the injection borehole at the beginning of fault instability to the pore pressure predicted by the failure criterion. It can be shown that the fluid overpressure is related to initial normal stress, shear stress and injection rate (Ji & Wu, 2020; Ji et al., 2021; Passelègue et al., 2018). However, for a critically stressed fault, the Mohr-Coulmb failure criterion predicts a

fluid pressure of 0, and the overpressure ratio of the fault cannot be calculated. Moreover, the fault overpressure ratio is strongly influenced by the fault initial stress state. Even for the same fault, different overpressure ratios might be obtained under different stress states. Therefore, we only study the effect of the overpressure on the reactivation of faults. Considering the effect of overpressure(P_{over}), the pore pressure effective stress criterion can be modified as:

$$\begin{cases} \sigma_{en} = \sigma_n & , P_w \le P_{over} \\ \sigma_{en} = \sigma_n - \overline{P_w} - P_{over} & , P_w > P_{over} \end{cases} \quad (17)$$

where $\overline{P_w}$ is the equivalent pore pressure in the fault.

The fluid overpressure is constant when the fluid distribution is uniform on faults and increases with a more heterogeneous fault pressure distribution as demonstrated by Passelègue et al. (2018). The fluid pressure distribution on a fault depends on the balance between fluid injection and diffusion rates (Ji et al., 2022). A faster rate of fluid injection promotes high gradients around the injection point (Ji & Wu, 2020; Ji et al., 2021; Passelègue et al., 2018). The rate of fluid injection can be artificially controlled. However, the heterogeneous fault pressure distribution is related to heterogeneity of the fault itself. As shown in Figure 10, the slip zone has a high pore pressure and is reactivated during the injection. The remainder of the fault remains locked. In the initial stage of fluid injection, although the pore pressure in the injection boreholes is gradually increased, the locked area retains the fault stable.

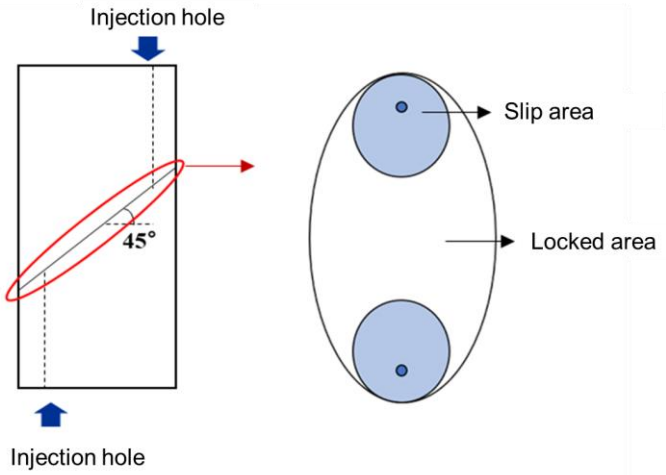

Figure 10. Locked and slipping zones on faults. The blue area is the slip area embedded within the (white) locked area.

The rate of pressure diffusion within the fault as expressed by the diffusion coefficient *A*, defined as:

$$A = k / \mu\alpha\Phi \quad (18)$$

where μ is fluid viscosity, α is fluid compressibility, Φ is the fault porosity and k is the fault permeability. As the fluid compressibility and dynamic viscosity, together with the fault porosity of each rock sample have the same value, the fault diffusion coefficient is a function of permeability. Therefore, the rate of pressure diffusion could also be characterized by permeability, which is an extremely important property for EGS projects. The relationship between overpressure and fault permeability, measured before fluid-pressure-driven reactivation, is shown in Figure 11 as a negative exponential relationship between the overpressure P_{over} and fault permeability k.

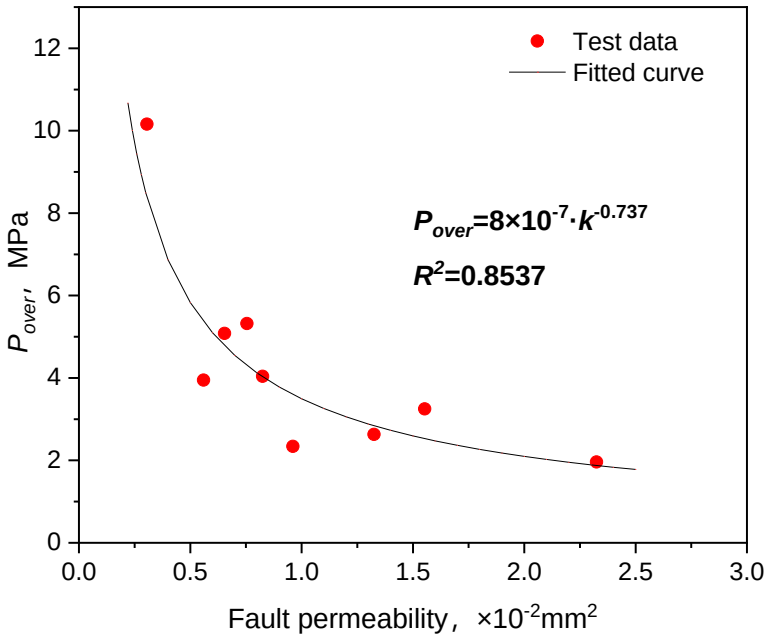

Figure 11. Fluid overpressure and fault permeability recovered from first slip on faults that exhibited significant stick-slip.

The mechanism of fault slip under pressure-drive is shown in Figure 12. During fluid injection, the shear stress produced by faults did not change in the initial stage due to the presence of overpressure, but decreased with the decreasing effective normal stress after the pore pressure exceeded the overpressure. The fault exhibited stick–slip response due to the combined mechanical and fluid loads during the increase of pore pressure, and a stress drop occurred. Subsequently, the stress path exhibits nonlinearity due to slip-strengthening and permeability evolution. During the strengthening process, the fluid pressure again increases, leading to continuous stick-slip response

in the smooth faults. The evolution of friction coefficient and permeability are the main factors influencing fluid-injection-induced earthquakes and are both related to fault roughness.

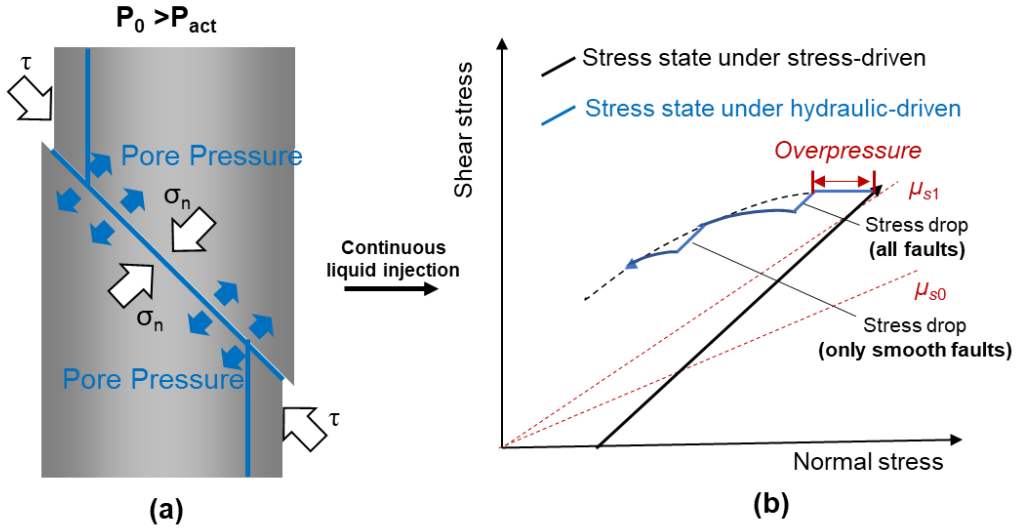

Figure 12. Mechanism of faults reactivation under fluid-pressure-drive -driven: (a) Schematic of fault instability; (b)Stress path of faults slip under fluid-pressure-driven.

4.3 Implications for injection-induced seismicity

During fluid injection, the fault is subjected to the combined effects of both stress and fluid pressure. It is important to fully understand the mechanisms of stress- and fluid-pressure-driven fault reactivation for the better assessment and control of induced earthquakes. We obtain the frictional slip characteristics of faults under stress- and fluid-pressure-driven conditions through a series of triaxial shear tests. The fault frictional slip characteristics are shown to be closely related to the roughness and permeability of the fault.

By comparing the stress- and hydraulic-driven fault slip characteristics, it is observed that under stress-driven conditions, stick–slips occurred only on the smoother faults. However, natural faults with a rougher surface showed stick–slip only at very high stress levels. For fluid injection, even the rough faults showed stick–slip response. This indicates that the risk of inducing earthquakes is extremely high once the fault slips as a result of fluid injection. For example, the Duvernay hydraulic fracturing project in Western Canada (Bao et al., 2016; Eyre et al., 2019a; Eyre et al., 2019b) and shale gas extraction in the central and eastern United States (Ellsworth et al., 2013;

Keranen et al., 2014;) and EGS projects in Switzerland (Elsworth et al., 2016; Majer et al., 2007), and South Korea (Kim et al., 2018; Grigoli et al., 2018) have all generated induced earthquakes.

At present, our determination of fault state is mainly based on the Mohr-Coulmb failure criterion and effective stress criterion. Fault slip is mainly influenced by the applied stresses and fault friction coefficient. For a fault in a critical state, the effective stress will decrease after liquid injection and the fault should slip immediately. However, the results of fluid injection induced seismicity in the central United States indicates that seismicity occurs potentially long after the injection (Keranen et al., 2013). This is potentially due to the uneven distribution of pore pressure within the fault, resulting in the fluid pressure required for fault activation often being higher than the value predicted by applying the Mohr-Coulmb failure criterion. The difference is the overpressure, making it difficult to determine the timing of injection-induced seismicity. During the injection, the pore pressure distribution in the fault is affected by various factors such as fault roughness, stress state, mineral composition, and fluid injection conditions (Fang & Wu, 2022), resulting in a complex behavior. This experimental study shows that the overpressure required for fault reactivation is related to its permeability. Fluid injection into EGS reservoirs will elevate permeability from micro- to milli-Darcy levels. This may reduce the pore pressure required for fault reactivation and increase the risk of induced earthquakes. Therefore, during EGS fluid injection, chemical and physical means can be used to stimulate the fault to increase its roughness, thereby reducing the risk of fluid injection induced earthquakes.

Finally, it is necessary to point out that the vast majority of previous studies on fluid injection induced earthquakes, whether from laboratory or field perspectives, focused more on the instability behavior of optimal faults under regional tectonic stress state. According to the Mohr-Coulmb criterion, the angle between the optimally orientated fault and the maximum principal stress is $45°–0.5\tan^{-1}\mu$. Byerlee (1978) indicated that for most rocks, the friction coefficient of the fault is ~0.6, corresponding to an optimal azimuth angle of ~30°. The 45° angle in this study is not the optimal fault orientation, regardless of the friction coefficients obtained from sawcut faults with various roughness. Due to the minimum shear stress required for the initiation of fault slip along the favorable direction, previous study results only provided the lower limit of fluid overpressure during fault slip (Ji et al., 2022). Hence, the results of our overpressure experiment may be more universally representative. It is necessary to pay more attention to the study of fluid injection induced earthquakes in unfavorably orientated faults in the future.

5 Conclusions

To obtain the slip characteristics of faults under both stress- and fluid-pressure-induced reactivation, we completed laboratory reactivation experiments on three groups of saw-cut faults with different roughnesses. The results show that under the stress-drive conditions, a rougher slips stably, suggesting slip strengthening and smoother faults reactivate in stick-slip mode - first exhibiting weak slip and then slip strengthening. Under pressure-driven condition, the uneven distribution of pore pressure results in fault slip only after the pore pressure within the fault increased to a significant overpressure. The magnitude of this overpressure is related to permeability with overpressure increasing with a decrease in permeability. The results potentially improve our ability to develop successful EGS projects and mitigate the risk of anthropogenic earthquakes in EGS.

Acknowledgments

The research was funded by National Natural Science Foundation of China (Nos. 42177175, 41807222), Central Public-interest Scientific Institution Basal Research Fund (No. DZLXJK202204), and China Geological Survey (Nos. DD20190138, DD20221660). Bin Li helped to make granite samples.

Data Availability Statement

This manuscript is accompanied by Supporting Information. The experimental data presented in this study are available at https://doi.org/10.5061/dryad.vt4b8gtws.

References

Aki, K. (1966). Generation and propagation of G waves from the Niigata earthquake of June 16, 1964. 2. Estimation of earthquake movement, released energy, and stress-strained drop from G wave spectrum. *Geology*, *44*(1),73-88,doi: 10.4236/ojer.2016.52007.

Andrews, D.J. (2013). *Objective Determination of Source Parameters and Similarity of Earthquakes of Different Size*. American Geophysical Union (AGU).

Bao, X., & Eaton, D. W. (2016). Fault activation by hydraulic fracturing in western Canada. *Science*, *354*(6318), 1406–1409, doi:10.1126/science.aag2583.

Bijay, K. C. , & Ghazanfari, E. (2021). Geothermal reservoir stimulation through hydro-shearing: an experimental study under conditions close to enhanced geothermal systems. *Geothermics*, *96*(5-6):102200, doi: 10.1016/j.geothermics.2021.102200.

Brace, W. F., Walsh J. B., & Frangos W. T.(1968). Permeability of granite under high pressure. *Journal of Geophysical Research, 73*(6), 2225-2236, doi: 10.1029/JB073i006p02225.

Byerlee, J. D. (1967). Frictional characteristics of granite under high confining pressure. *Journal of Geophysical Research, 72*(14), doi: 10.1029/JZ072i014p03639.

Cappa, F., Scuderi, M.M., Collettini, C., Guglielmi, Y., & Avouac, J.P. (2019). Stabilization of fault slip by fluid injection in the laboratory and in situ. *Science Advances, 5*(3), eaau4065, doi: 10.1126/sciadv. aau4065.

Cappa F., Guglielmi Y., Nussbaum C., De Barros L., & Birkholzer J. (2022). Fluid migration in low-permeability faults driven by decoupling of fault slip and opening. *Nature Geoscience*, *15*, 747–751, doi:10.1038/S41561-022-00993-4.

Chen, Y., Zhang, C., Zhao, Z., & Zhao, X. (2020). Shear Behavior of Artificial and Natural Granite Fractures After Heating and Water-Cooling Treatment. *Rock Mechanics and Rock Engineering*, *53*(4–5), 5429–5449, doi: 10.1007/s00603-020-02221-0.

Collettini, C. (2014). A novel and versatile apparatus for brittle rock deformation. *International Journal of Rock Mechanics and Mining Sciences*, *66*,114-123, doi: 10.1016/j.ijrmms.2013.12.005.

Cornelio, C., Spagnuolo, E., Di Toro, G., Nielsen, S., & Violay, M. (2019). Mechanical behaviour of fluid-lubricated faults. *Nature Communications*, *10*(1), 1274. doi: 10.1038/s41467-019-09293-9.

Dieterich, J. H. (1978). Time-Dependent Friction and the Mechanics of Stick-Slip. *pure and applied geophysics*, *116*(4), 790-806, doi:10.1007/BF00876539.

Dieterich, J.H. (1979). Modeling of rock friction: 1. Experimental results and constitutive equations. *Journal of Geophysical Research*. *84*(B5), 2161, doi: 10.1029/JB084IB05P02161.

Ellsworth, W.L. (2013). Injection-Induced earthquakes. *Science*, *341*(6142):1225942, doi: 10.1126/science.1225942.

Elsworth, D., Spiers J. C. & Niemeijer A. R. (2016). Understanding induced seismicity. Science, *6318*(354), 1380-1381, doi:10.1126/science.aal2584.

Eyre, T. S., Eaton, D. W., Megan, Z., David, D., & Danylo, K. (2019a). Microseismicity reveals fault activation before mw 4.1 hydraulic-fracturing induced earthquake. *Geophysical Journal International*, *218*(1):534–46, doi: 10.1093/gji/ggz168.

Eyre, T. S., Eaton, D. W., Garagash, D. I., Zecevic, M., & Lawton, D. C. (2019b). The role of aseismic slip in hydraulic fracturing-induced seismicity. *Science Advances*, *5*(8), eaav7172, doi: 10.1126/sciadv.aav7172.

Fang, Z., & Wu, W. (2022). Laboratory friction-permeability response of rock fractures: a review and new insights. *Geomechanics and Geophysics for Geo-Energy and Geo-Resources*. *8*(1), 15 ,doi:10.1007/s40948-021-00316-8.

Galis, M., Ampuero, J.P., Mai, P.M., & Cappa, F. (2017). Induced seismicity provides insight into why earthquake ruptures stop. *Science Advances*, *3*(12), 7528, doi:10.1126/sciadv.aap7528.

602 Grigoli, F., Cesca, S., Rinaldi, A. P., Manconi, A., López-Comino, J. A., & Clinton, J. F., et al. (2018). The
603 November 2017 Mw 5.5 Pohang earthquake: a possible case of induced seismicity in South Lorea. *Science*,
604 *360*(6392), 1003-1006, doi: 10.1126/science.aat2010.
605 Hao, M. Shen, Z., Wang, Q., & Cui, D. (2012). Postseismic deformation mechanisms of the 1990 Mw 6.4
606 Gonghe, China earthquake constrained using leveling measurements. *Tectonophysics*, 532–535, 205–214,
607 doi:10.1016/j.tecto.2012.02.005.
608 Ida, Y. (1972). Cohesive force across the tip of a longitudinal-shear crack and Griffith's specific surface energy.
609 *Journal of Geophysical Research*, *77*(20), 3796–3805, doi:10.1029/JB077i020p03796.
610 Ishibashi, T., Elsworth, D., Fang, Y., Riviere, J., Madara, B., Asanuma, H., Watanabe, N., & Marone, C. (2018).
611 Friction-Stability-Permeability Evolution of a Fracture in Granite. *Water Resources Research*, *54*(12), 9901–
612 9918, doi.:10.1029/2018WR022598.
613 Jaeger, J. C., Cook, N. G. W., & Zimmerman, R. (2009). *Fundamentals of rock mechanics*. John Wiley & Sons.
614 Ji, Y. , Hofmann, H. , Duan, K. , & Zang, A. (2022). Laboratory experiments on fault behavior towards better
615 understanding of injection-induced seismicity in geoenergy systems. *Earth-Science Reviews*, *226*(1),doi:
616 0.1016/j.earscirev.2021.103916.
617 Ji, Y., Fang, Z., & Wu, W. (2021). Fluid Overpressurization of Rock Fractures: Experimental Investigation and
618 Analytical Modeling. *Rock Mechanics and Rock Engineering*, *54*(6318), doi: 10.1007/s00603-021-02453-8.
619 Ji, Y., Wanniarachchi, W.A.M., & Wu, W. (2020). Effect of fluid pressure heterogeneity on injection-induced
620 fracture activation. *Computers and Geotechnics*, *123*(6318), 103589, doi: 10.1016/j.compgeo.2020.103589.
621 Ji, Y., & Wu, W. (2020). Injection-driven fracture instability in granite: Mechanism and implications.
622 *Tectonophysics*, *791*(B12), 228572, doi: 10.1016/j.tecto.2020.228572.
623 Ji, Y. . (2020). *Shear-flow characteristics of rock fractures and implications for injection-induced seismicity*.
624 Ph.D. Nanyang Technological University, doi: 10.32657/10356/143989.
625 Ji, Y. , Wu, W., & Zhao, Z. (2019). Unloading-induced rock fracture activation and maximum seismic moment
626 prediction. *Engineering Geology*, *262*(6), doi: 10.1016/j.enggeo.2019.105352.
627 Jia, Y., Wu, W., & Kong, X.Z. (2020). Injection-induced slip heterogeneity on faults in shale reservoirs.
628 *International Journal of Rock Mechanics and Mining Sciences*, *131*(3), 104363, doi:
629 10.1016/j.ijrmms.2020.104363.
630 Kakurina, M., Guglielmi, Y., Nussbaum, C., & Valley, B. (2019). Slip perturbation during fault reactivation by
631 a fluid injection. *Tectonophysics*, *757*, 140–152, doi: 10.1016/j.tecto.2019.01.017.
632 Keranen, K. M., Savage, H. M., Abers, G. A., & Cochran, E. S. (2013). Potentially induced earthquakes in
633 Oklahoma, USA: Links between wastewater injection and the 2011 Mw 5.7 earthquake sequence. *Geology*,
634 *41*(6), 699-702,doi: 10.1130/G34045.1
635 Kim, K. H., Ree, J. H., Kim, Y. H., Kim, S., Kang, S. Y., & Seo, W. (2018). Assessing whether the 2017 Mw
636 5.4 Pohang earthquake in South Lorea was an induced event. *Science*, *360*(6392), 1007-1009, doi:
637 10.1126/science.aat6081.

638 Lengliné, O., Boubacar, M., & Schmittbuhl, J. (2017). Seismicity related to the hydraulic stimulation of GRT1,
639 Rittershoffen, France. *Geophysical Journal International*, 208(3):ggw490, doi:10.1093/gji/ggw490.
640 Majer, E. L., Baria, R., Stark, M., Oates, S., Bommer, J., & Smith, B., et al. (2007). Induced seismicity associated
641 with enhanced geothermal systems. *Geothermics*, *36*(3), 185-222, doi: 10.1016/j.geothermics.2007.03.003.
642 Maurer, J., & Segall, P., 2018. Magnitudes of Induced Earthquakes in Low-Stress Environments. *Bulletin of the*
643 *Seismological Society of America*, *108*(3), 1087–1106, doi: 10.1785/0120170295.
644 Mclaskey, G. C., & Yamashita, F. (2017). Slow and fast ruptures on a laboratory fault controlled by loading
645 characteristics. *Journal of Geophysical Research: Solid Earth*, *122*(5), doi: 10.1002/2016JB013681.
646 Mohammadioun, B. (2001). Stress Drop, Slip Type, Earthquake Magnitude, and Seismic Hazard. Bull Seismol
647 Soc Amer, *91*(4), 694–707, doi: doi.org/10.1785/0120000067.
648 Palmer, A.C., & Rice, J.R. (1973). The Growth of Slip Surfaces in the Progressive Failure of Over-Consolidated
649 Clay. *Proceedings of The Royal Society a Mathematical Physical and Engineering Sciences*, *332*(1591):527-
650 548, doi: 10.1098/rspa.1973.0040.
651 Passelègue, François.X., Brantut, N., & Mitchell, T.M. (2018). Fault Reactivation by Fluid Injection: Controls
652 From Stress State and Injection Rate. *Geophysical Research Letters*, *45*(23), doi: 10.1029/2018GL080470.
653 Passelègue, François.X., Schubnel, A. , Nielsen, S. , Bhat, H. , Deldicque, D. , & Raùl Madariaga, et al. (2019).
654 Dynamic rupture processes inferred from laboratory microearthquakes. *Journal of Geophysical Research:*
655 *Solid Earth*, 121(6), doi: 10.1002/2015JB012694.
656 Ruina, A. (1983). Slip instability and state variable friction laws. *Journal of Geophysical Research: Solid Earth,*
657 *88*(B12), 10359–10370, doi: 10.1029/JB088iB12p10359.
658 Rutter, E., & Hackston, A. (2017). On the effective stress law for rock-on-rock frictional sliding, and fault slip
659 triggered by means of fluid injection. *Philosophical Transactions of The Royal Society A Mathematical*
660 *Physical and Engineering Sciences*, *375*(2103):20160001, doi: 10.1098/rsta.2016.0001.
661 Scholz, C., Molnar, P., & Johnson, T. (1972). Detailed studies of frictional sliding of granite and implications
662 for the earthquake mechanism. *Journal of Geophysical Research*, *77*(32), 6392-6406, doi:
663 10.1029/JB077i032p06392.
664 Tembe, S. , Lockner, D. A. , & Wong, T. . (2010). Effect of clay content and mineralogy on frictional sliding
665 behavior of simulated gouges: binary and ternary mixtures of quartz, illite, and montmorillonite. *Journal of*
666 *Geophysical Research*: *Solid Earth*, *115*(B3), doi: 10.1029/2009JB006383.Tsutsumi, A., & Shimamoto, T.
667 (1997). High-velocity frictional properties of gabbro. *Geophysical Research Letters*, *24*(6):699-702, doi:
668 10.1029/97GL00503.
669 Ujiie, K., & Tsutsumi, A. (2010). High-velocity frictional properties of clay-rich fault gouge in a megasplay
670 fault zone, Nankai subduction zone. *Geophysical Research Letters*, *37*(24), doi: 10.1029/2010GL046002.
671 van der Elst, N.J., Page, M.T., Weiser, D.A., Goebel, T.H.W., & Hosseini, S.M., 2016. Induced earthquake
672 magnitudes are as large as (statistically) expected: Induced earthquake maximum magnitudes. *Journal of*
673 *Geophysical Research*: *Solid Earth*, *121*(6), 4575–4590, doi: 10.1002/2016JB012818.

Vogler, D. , Amann, F. , Bayer, P. , & Elsworth, D. (2016). Permeability evolution in natural fractures subject to cyclic loading and gouge formation. *Rock Mechanics&Rock Engineering* ,*49*(9), doi: 10.1007/s00603-016-1022-0.

Wang, L., Kwiatek, G., Rybacki, E., Bonnelye, A., Bohnhoff, M., & Dresen, G. (2020). Laboratory Study on Fluid-Induced Fault Slip Behavior: The Role of Fluid Pressurization Rate. *Geophysical Research Letters*. *47*(6), doi: 10.1029/2019GL086627.

Wu, W., Reece, J.S., Gensterblum, Y., & Zoback, M.D. (2017). Permeability Evolution of Slowly Slipping Faults in Shale Reservoirs. *Geophysical Research Letters*, *44*(24), 11368-11375, doi:10.1002/2017gl075506.

Ye, Z., & Ghassemi, A. (2018). Injection-Induced Shear Slip and Permeability Enhancement in Granite Fractures. *Journal of Geophysical Research*: *Solid Earth*, *123*, 9009–9032, doi: 10.1029/2018JB016045.

Yu F., Arnaud M., Didier S., Ke G.(2022). Investigating Injection Pressure as a Predictor to Enhance Real-Time Forecasting of Fluid-Induced Seismicity: A Bayesian Model Comparison. *Seismological Research Letters*,1-22, doi: https://doi.org/10.1785/0220220309

Zhao, Q., Tisato, N., Kovaleva, O., & Grasselli, G.(2018a). Direct Observation of Faulting by Means of Rotary Shear Tests Under X-Ray Micro-Computed Tomography. *Journal of Geophysical Research*: *Solid Earth*, *123*(9),7389–7403, doi: 10.1029/2017JB015394.

Zhao, Z., Peng, H., Wu, W., & Chen, Y. F. (2018b). Characteristics of shear-induced asperity degradation of rock fractures and implications for solute retardation. *International Journal of Rock Mechanics and Mining Sciences*, *105*, 53–61, doi: 10.1016/j.ijrmms.2018.03.012.

Zhang, E. et al. (2022). The first power generation test of hot dry rock resources exploration and production demonstration project in the Gonghe Basin, Qinghai Province, China, *China Geology*, 5(3), 372–382, doi:10.31035/cg2022038.